THE ASTROPHYSICAL JOURNAL, 373:509–524, 1991 June 1

ON THE DISPERSION IN DIRECTION OF INTERSTELLAR POLARIZATION

P. C. MYERS
Harvard-Smithsonian Center for Astrophysics, Mail Stop 42, 60 Garden Street, Cambridge, MA 02138
AND
A. A. GOODMAN
Astronomy Department, Campbell Hall, University of California, Berkeley, CA 94720
Received 1990 October 12; accepted 1990 November 16

ABSTRACT

Optical polarization maps of 15 dark clouds, five clusters, and six complexes are analyzed to study the spatial patterns and number distributions of the direction of interstellar optical polarization. Most clouds have a well-defined mean direction over their spatial extent, or two or three spatial zones with distinctly different mean directions. Their number distributions of polarization direction generally have a single local maximum, with dispersion 0.2–0.4 radians. Clouds with embedded star clusters have distributions with greater breadth and different mean direction than those of neighboring clouds with less extinction and fewer young stars. Clouds with embedded clusters have median dispersion 0.4–0.5 radians, while clouds without embedded clusters have median dispersion 0.2–0.3 radians. The enhanced dispersion of embedded clusters may be more closely associated with the dense gas than with the young stars in the cluster. If so, the increased dispersion may result from gas accumulation with infall speed slightly greater than the Alfvén speed.

The observed distribution of polarization angle is modeled as arising from a magnetic field with uniform and nonuniform parts. The nonuniform part has an isotropic probability distribution of direction, a Gaussian distribution of amplitude, and N correlation lengths along the line of sight through the cloud. The model fits observed distributions of polarization angle in terms of the mean polarization angle and the dispersion about the mean. The model estimates the three-dimensional uniform field, and its inclination to the line of sight, by combining maps of polarization direction and maps of the line-of-sight field component, based on the Zeeman effect. In L204, these quantities are 6 μG and 47°. The uniform and nonuniform components of magnetic energy density are comparable if the typical cloud has a few correlation lengths along the line of sight. This requirement on N is consistent with the spatial patterns of several optical polarization maps, and with the estimated upper limit $N_{\rm max} \simeq 10$, based on the cutoff wavelength of hydromagnetic waves.

Subject headings: clusters: open — interstellar: magnetic fields — interstellar: matter — polarization

1. INTRODUCTION

Since the discovery of the polarization of optical starlight (Hiltner 1949; Hall 1949), thousands of measurements have been reported of the direction and magnitude of polarization along lines of sight toward stars in the Galaxy (e.g., Hiltner 1956; Mathewson & Ford 1970). Such polarization is widespread and well documented. It is generally attributed to differential scattering of unpolarized starlight by elongated dust grains, whose spin axes tend to align with the interstellar magnetic field (Davis & Greenstein 1951; Jones & Spitzer 1967; Purcell & Spitzer 1971; Purcell 1979). A detailed review of polarization mechanisms is given by Hildebrand (1988).

The earliest polarization observations showed that the direction of polarization has significant coherence over 100–1000 pc, but it is not perfectly uniform, even in regions where systematic contributions due to curvature of galactic arms should be negligible (Hiltner 1956). The typical rms dispersions of direction in these measurements, 0.1–0.2 radians, is much greater than measurement uncertainty, and thus may contain information about the nonuniform component of the interstellar magnetic field.

Several efforts have been made to interpret the dispersion in polarization direction, which we denote as σ_{θ_E}. Davis (1951) and Chandrasekhar & Fermi (1953) modeled σ_{θ_E} as arising from wavelike distortions in the Galactic magnetic field due to the turbulent relative motions of separate gas clouds, yielding estimates of field strength of a few microgauss. Jokipii & Parker (1969) emphasized the stochastic nature of astrophysical magnetic fields, and described σ_{θ_E} as an approximate measure of the relative value of the dispersion in the field, σ_B, with respect to the mean field B.

More recently, it has become possible to study the role of the magnetic field in individual clouds, owing to progress in measurement of the Zeeman effect in spectral lines of H I and OH (Heiles 1987). In most cases the observed field strength lies within a factor of 2 of the value expected from equipartition between magnetic, gravitational, and kinetic energy (Myers & Goodman 1988a, b). At the same time, many detailed observations have been made of the optical polarization toward and around dark clouds and dark cloud complexes (Vrba, Strom, & Strom 1976; McDavid 1984; McCutcheon et al. 1986; Heyer et al. 1987; Vrba, Strom, & Strom 1988; Goodman et al. 1990). As with the earlier measurements on the Galactic scale, these observations show typical dispersion in position angle of a few tenths of a radian, but now on a much smaller scale of angular and linear position.

Therefore, it is now both desirable and possible to analyze polarization data quantitatively for individual clouds, to obtain information on their associated magnetic fields. Recently Zweibel (1990) has extended the treatment of Chandrasekhar & Fermi (1953) to individual clouds, under various conditions of ionization, clumping, and ambipolar diffusion.

Jones (1989) has modeled the depolarizing effect of fields that vary randomly along the line of sight.

In this paper we extend the statistical description of Jokipii & Parker (1969). We model the distribution in polarization angle as arising from magnetic fields with uniform and nonuniform components, where the nonuniform component is nonuniform both along and across the line of sight. The model distribution is fitted to each of 26 observed distributions. The best-fit dispersion is used to distinguish embedded star clusters, which tend to have large dispersion, from quiescent dark clouds, which tend to have small dispersion. The dispersion is used to estimate the relative energy density in the uniform and nonuniform field components. These values appear comparable to each other for most clouds. For the dark cloud Lynds 204, these estimates are combined with Zeeman measurements to estimate the magnitude and inclination angle of the three-dimensional uniform field associated with the cloud.

The models presented here are not restricted to optical polarization, but with slight modification can also apply to the polarized infrared emission from magnetically aligned grains, and to the polarized synchrotron emission from the magnetized plasma observed in external galaxies.

Section 2 presents and describes available measurements of optical polarization toward some 20 dark cloud regions. Section 3 presents models of the polarization distribution. Section 4 compares the observed and model distributions, and combines polarization data and Zeeman effect data to estimate the magnitude and inclination angle of the three-dimensional uniform field component for L204. Section 5 discusses implications and limitations of the data and models. Section 6 summarizes the paper.

2. POLARIZATION DATA

2.1. *Organization*

The polarization data presented here are organized so as to reveal the variation in width of the number distributions of position angle, over a factor of about 5 from the Lupus 4 dark cloud to the Corona Australis dark cloud complex. Accordingly, the data are grouped into three types of region: (*a*) individual dark clouds with relatively modest star formation; (*b*) clouds with prominent star clusters, defined here to contain more than 15 associated stars in an area of 1 pc^2; and (*c*) dark cloud complexes with at least two individual dark clouds, each separated from its nearest neighbor by at most a few times its size. The regions are divided into clouds with and without clusters because clusters seem to have significantly broader distributions than do clouds without clusters, as is discussed in § 2.4 below. The regions are divided into clouds and complexes because the complexes usually have broader distributions than do their individual cloud members. Within each group, regions are presented in order of increasing histogram width.

2.2. *Editing*

Forty-eight measurements were deleted from the original references, to exclude 1 σ uncertainties in position angle greater than 15°. In most cases, the uncertainty is smaller than 5°. For the Perseus cluster NGC 1333, the dark clouds B1 + B3 + B5 extending to the east, and for the entire Perseus complex, additional measurements with less than 1.1% polarization were deleted, to exclude one peak of a bimodal distribution. This distribution is likely due to the presence of more than one cloud complex along the line of sight (Goodman et al. 1990). This threshold value was chosen to exclude as much of the smaller polarization component as possible, without too large a sacrifice in statistical significance. A similar procedure was employed by Vrba et al. (1988) for the L1641 cloud, which, like the Perseus complex, shows a bimodal distribution of polarization angle before correction.

For three regions with clusters, the polarization data were divided to examine the difference between the polarization of background stars close to the cluster and the polarization of background stars farther from the cluster, but still close to the cloud complex that contains the cluster. Thus, data for the "HD 147889" cluster in Ophiuchus are from Vrba et al. (1976), but consist only of those within the 1°6 × 1°5 rectangle specified in Table 1, centered on the cluster described by Wilking, Lada, & Young (1989). Data for B1 + B3 + B5 in Perseus were obtained from those reported by Goodman et al. (1990) by excluding measurements east of right ascension 03^h28^m, the eastern border of the 0°8 × 0°8 square centered on the cluster NGC 1333, for which detailed measurements were reported by Vrba et al. (1976). (We did not include the polarization measurements in NGC 1333 presented by Turnshek, Turnshek, & Craine 1980, because they are too few in number.) Data for the NGC 6726 cluster in Corona Australis were obtained from those reported by Vrba, Coyne, & Tapia (1981, hereafter VCT), within a 1°5 × 1°5 square centered on VCT star 81. Data for the neighboring dark cloud, which was called GF 23 B1, B2, C1, and C2 by Schneider & Elmegreen (1979), were also taken from VCT.

2.3. *Presentation*

Table 1 presents polarization information (*a*) on 15 dark clouds that lack prominent star clusters, and (*b*) on five clusters, and (*c*) on six cloud complexes. These comprise essentially all such regions having at least about 30 reliable measurements of optical polarization. Each cluster is denoted by its NGC name or by the name of its brightest optically visible star.

Each region in Table 2 is described by the approximate boundaries enclosing the positions where polarization was measured, the number of such measurements, and three quantities describing the distribution of polarization.

The parameters $\bar{\Theta}_E$ and s in Table 1 are, respectively, the mean and dispersion of the distribution, based on least-squares fits of the model f^{3D}, to be described in § 3 and in § 4.1. Within Tables 1A, 1B, and 1C, regions are arranged in order of increasing s. The "spatial pattern type" describes the spatial arrangement of the polarization directions in a cloud map, according to the following scheme:

1. A single mean direction, and a spatially uniform dispersion about the mean, over the entire region (Lupus 4, Chamaeleon 2, Chamaeleon 1, L1755, B216, GF 23, Chamaeleon complex, Lupus complex).
2. Two distinct directions, with similar dispersions, over the entire region (L1506, Perseus complex; for the latter region, the second component may arise in a second cloud along the line of sight).
3. Two or more distinct directions, each in a zone distinct from its neighbors (GF 7, B18, L204, L1641, Lupus 3, Taurus complex).
4. Two zones with distinctly different dispersion, and with a clear direction only in the small-dispersion zone (Lupus 2, Ophiuchus complex, Corona Australis complex).
5. Large dispersion with no distinct direction (L1689, N1333).

TABLE 1

DISTRIBUTIONS OF OPTICAL POLARIZATION ANGLE

REGION (1)	R.A.(1950) Minimum (2)	R.A.(1950) Maximum (3)	Decl.(1950) Minimum (4)	Decl.(1950) Maximum (5)	N_{tot} (6)	$\bar{\Theta}_E$ (7)	s (8)	SPATIAL PATTERN TYPE (9)	REFERENCES (10)
A. Clouds without Clusters									
Lupus 4	$15^h53^m.3$	$16^h05^m.8$	−42°30′	−41°20′	42	22° ± 1°	0.16 ± 0.01	1	1
Chamaeleon 2	12 51.5	13 05.8	−77 40	−76 40	79	117 ± 1	0.18 ± 0.01	1	1
GF 7	20 53.2	21 06.8	46 30	50 20	29	31 ± 1	0.18 ± 0.02	3	2
L1755	16 36.0	16 46.0	−22 30	−21 00	48	58.6 ± 0.4	0.21 ± 0.01	1	3
Chamaeleon 1	10 50.9	11 12.0	−77 40	−75 45	124	125 ± 1	0.22 ± 0.01	1	1
B18	04 22.2	04 33.9	23 20	25 20	62	55 ± 1	0.23 ± 0.01	3	4
B216	04 15.1	04 26.2	25 55	27 45	57	28 ± 1	0.26 ± 0.01	1	4
B1 + B3 + B5	03 28.0	03 48.0	29 50	32 50	32	147 ± 3	0.27 ± 0.04	2	3
L1506	04 15.0	04 22.0	24 40	25 25	38	77 ± 1	0.30 ± 0.02	2	3
GF 23	19 00.9	19 09.5	−38 15	−36 45	29	90 ± 2	0.37 ± 0.02	1	5, 6
L204	16 43.3	16 48.0	−14 20	−09 20	49	71 ± 2	0.40 ± 0.03	3	7
L1641	05 32.3	05 42.6	−09 45	−06 05	71	121 ± 3	0.42 ± 0.04	3	8
Lupus 1	15 34.6	15 44.9	−35 13	−33 00	98	50 ± 2	0.43 ± 0.04	3	1
Lupus 2	15 51.8	15 58.6	−38 00	−37 05	54	40 ± 5	0.5 ± 0.1	4	1
L1689	16 27.0	16 33.0	−25 30	−24 00	29	61 ± 8	0.7 ± 0.1	5	9
B. Clusters									
α Per	02 40.0	03 35.0	45 00	52 00	83	118 ± 1	0.29 ± 0.01	1	10
HR 5999	15 59.2	16 12.3	−39 26	−38 17	54	178 ± 1	0.32 ± 0.02	3	1, 11
HD 147889	16 20.0	16 27.0	−25 00	−23 30	32	40 ± 4	0.4 ± 0.1	3	9, 12
NGC 1333	03 24.1	03 27.6	30 45	31 35	38	98 ± 7	0.5 ± 0.1	5	9
NGC 6726	18 54.5	19 00.9	−38 15	−36 45	32	52 ± 16	0.9 ± 0.3	5	5, 13
C. Complexes									
Chamaeleon	(Chamaeleon 1 + Chamaeleon 2)				203	121.1 ± 0.4	0.22 ± 0.01	1	1
Ophiuchus	16 19.0	16 46.0	−25 15	−21 00	166	54 ± 2	0.34 ± 0.03	4	3, 9
Taurus	04 15.0	04 54.0	22 00	30 00	339	48 ± 1	0.43 ± 0.01	3	3, 4, 14
Lupus	(Lupus 2 + HR 5999 + Lupus 4)				150	16 ± 2	0.47 ± 0.03	...	1, 15
Perseus	03 20.5	03 46.0	29 50	32 50	41	149 ± 9	0.7 ± 0.1	2, 5	3
Corona Australis	(NGC 6726 + GF 23)				61	86 ± 6	0.9 ± 0.1	4	5, 13, 16

REFERENCES.—(1) Vrba et al. 1991; (2) McDavid 1984; (3) Goodman et al. 1990; (4) Heyer et al. 1987; (5) Vrba et al. 1981; (6) Schneider & Elmegreen 1979; (7) McCutcheon et al. 1986; (8) Vrba et al. 1988; (9) Vrba et al. 1976; (10) Coyne et al. 1979; (11) Schwartz 1977; (12) Wilking et al. 1989; (13) Taylor & Storey 1984; (14) Moneti et al. 1984; (15) Krautter 1990.

NOTE.—For each region, the description of the spatial and number distributions of polarization angle Θ_E are based on the number N_{tot} of measurements listed in col. (6), with the region boundaries indicated in cols. (2)–(5). The mean polarization angle $\bar{\Theta}_E$ in col. (7), the dispersion s in col. (8), and their 1 σ uncertainties, are based on least-squares fits to eq. (18). The spatial distribution of polarization angles in each region is classified in col. (9), according to the scheme described in § 2.3 and illustrated in Fig. 1.

A "cloud" is defined by a relatively continuous distribution of visible obscuration. It has an "embedded cluster" if there are more than 15 associated stars in the area of 1 pc^2. Clusters are named by their NGC name, or else by the name of their brightest optically visible member. Clouds are considered to belong to "complexes" if the projected cloud-cloud separation is no more than a few cloud diameters and if there is evidence of collocation from distance estimates for associated stars and/or from molecular line velocities.

These five patterns are illustrated in Figure 1, which shows position-angle maps for L1755; the Perseus complex; the Lupus 3 cloud, which contains the HR 5999 cluster; the Corona Australis complex; and the NGC 1333 cluster. The references for these examples are cited in the note to Table 1. In most cases the original references also show the relation of the polarization map to the visual extinction. These pattern definitions are qualitative and not unique, so some assignments of patterns to clouds are subjective. Nonetheless, the definitions serve as a guide to the range of patterns observed. Types 1 and 3 are the most common.

Figures 2, 3, and 4 show number distributions of polarization angle Θ_E for the regions listed in Tables 1A, 1B, and 1C, respectively. They are presented with bin boundaries at integer multiples of 10°, measured as usual counterclockwise from north. Each plot is centered approximately at the mean position angle $\bar{\Theta}_E$. Due to this centering, Θ_E extends beyond its usual range of 0°–180°. Therefore, values of Θ_E greater than 180° are equivalent to $\Theta_E - 180°$, and values of Θ_E less than 0° are equivalent to $\Theta_E + 180°$.

We tested whether the distributions in Figures 2–4 change if bin boundaries are shifted by half a bin, or if bin widths of 15° are used instead of 10° as in Figures 2–4. In neither case do the distributions differ significantly in mean position angle, width, or shape from those in Figures 2–4.

2.4. *Polarization Distributions in Clouds and Clusters*

In nearly all clouds, the distribution of position angle shows a single, well-defined local maximum, with dispersion s ranging from 0.16 for the Lupus 4 cloud to 0.7 for L1689. Only two regions have clearly bimodal distributions, the L1641 cloud in Orion (Vrba et al. 1988) and the B1 + B3 + B5 cloud in Perseus (Goodman et al. 1990). In each of these two regions, the two components of the bimodal distribution of direction have distinctly different percentage polarization. The less pol-

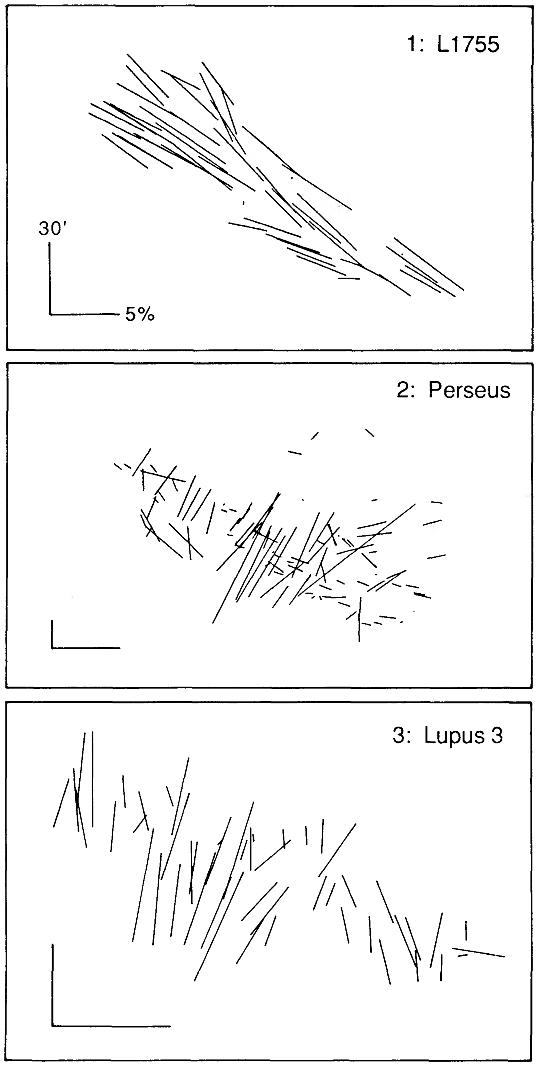

FIG. 1*a*

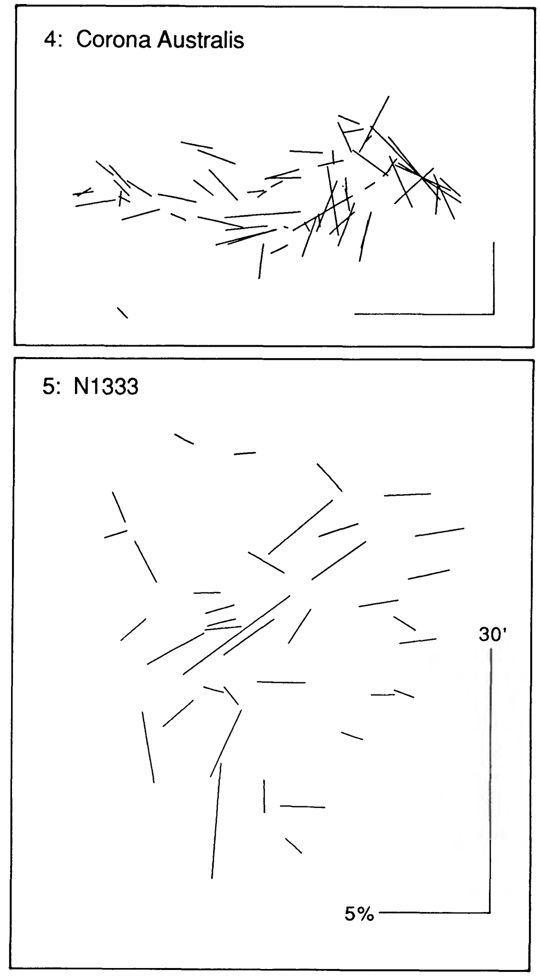

FIG. 1*b*

FIG. 1.—Polarization maps of five regions, illustrating the "spatial pattern types" described in § 2.3. (*a*) Maps of the L1755 cloud (spatially uniform mean and dispersion in direction), the Perseus complex (two distinct directions over the entire region), and the Lupus 3 cloud, which contains the HR 5999 cluster (two or more spatial zones, each with a distinct direction). (*b*) Maps of the Corona Australis complex (two zones with distinctly different dispersion) and the NGC 1333 cluster (large dispersion, with no clear direction).

arized component probably arises in a foreground region, as discussed in detail by Vrba (1988).

The most prominent difference in position-angle distribution among the regions considered here appears to arise between clouds with embedded clusters and other comparable regions. All four of the clouds with embedded star clusters in Table 1B have distributions substantially broader than in each of their near-neighbor clouds. In Ophiuchus, the HD 147889 region has $s = 0.4$, while the filamentary clouds L1709 and L1755, which extend to the northeast from the cluster, together have $s = 0.23$. In Perseus, the NGC 1333 region has $s = 0.5$, while the region B1 + B3 + B5 extending to the east has $s = 0.27$. In Corona Australis, the NGC 6726 region has $s = 0.9$, while GF 23 extending to the east has $s = 0.37$. These three pairs of distributions are shown in Figure 5*a*. There the broadening of the distribution from cloud to cluster is evident. In addition, the mean position angle of each cluster distribution is clearly shifted with respect to that of its neighboring cloud. We have examined these pairs for statistical distinctness with the Kolmogorov-Smirnov two-sample, two-tailed test (Siegel 1956). For each pair, the hypothesis that its two distributions are samples of the same population is rejected at the 5% level or better. The fourth embedded cluster, HR 5999 in the Lupus 3 cloud, also shows increased dispersion of polarization angle compared with its filamentary dark cloud extending to the east. But it has too few polarization measurements for detailed quantitative comparison.

Furthermore, the cluster dispersions are generally broader than those of the typical dark cloud without a cluster, not just those dark clouds lying near the cluster. The median dispersion for the four embedded clusters is $s = 0.4$–0.5, while the median dispersion for the 16 clouds without clusters in Table 1A is $s = 0.26$–0.28.

The embedded cluster dispersion ($s = 0.32$, 0.4, 0.5, and 0.9) are also broader than that ($s = 0.29$) of the much more developed, but less obscured, cluster α Persei. This cluster has about 200 stars, with typical visual extinction only 0.3 mag (Coyne, Tapia, & Vrba 1979). If this difference in polarization disper-

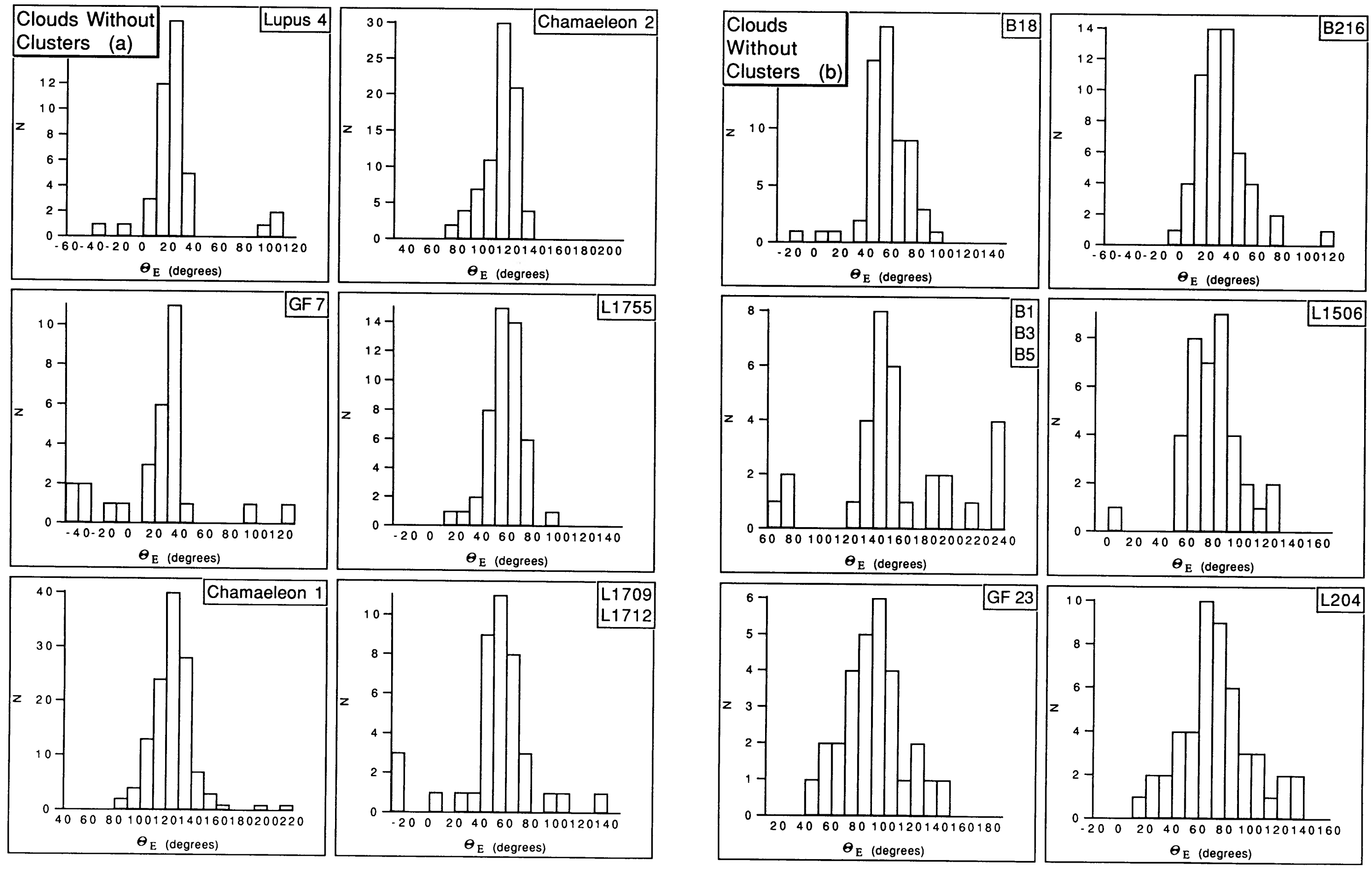

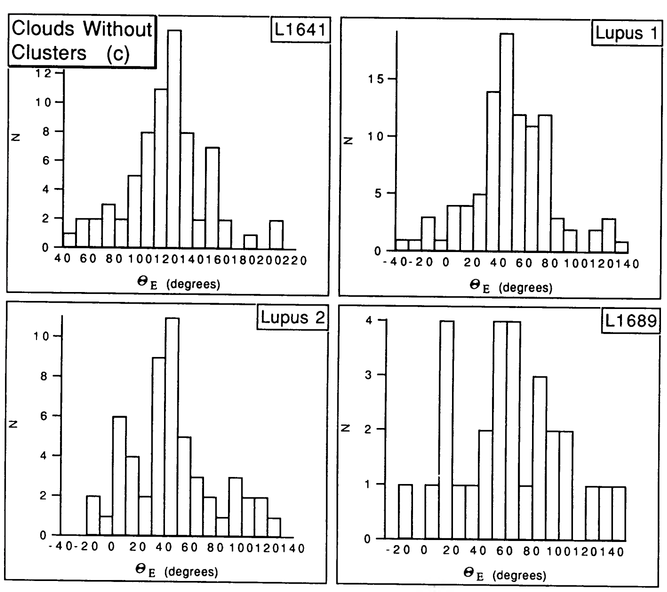

FIG. 2.—Number distributions of polarization angle for 15 dark clouds without embedded star clusters, arranged in order of increasing dispersion s.

sion is representative of larger samples, it implies that the large dispersion in position angle for embedded clusters cannot be attributed simply to the total number of stars in the cluster. Instead, the presence of young stars, and/or the presence of substantial gas and dust, seems more consistent with the available data as a cause for large dispersion.

To test whether the large dispersion for embedded clusters arises from effects of stars or from associated dense gas, we consider L1689 in Ophiuchus. This dark cloud has mass 570 $M_\odot$ according to its ^{13}CO emission, second only to L1688, which contains the HD 147889 cluster, with 1400 $M_\odot$ (Loren 1989). Both regions are visually opaque. But within the boundaries specified in Table 1, L1689 contains only five optically invisible embedded *IRAS* point sources, while L1688 contains 24 (Ichikawa & Nishida 1989). Thus L1689 is a cloud that resembles small embedded clusters in its mass and extinction but not (or perhaps not yet) in its stellar content. The polarization dispersion of the L1689 region, 0.7 ± 0.1, is comparable to that of the cluster regions. It is the largest dispersion of the clouds without clusters, and is greater than that of its neighboring filamentary cloud L1712, for which $s = 0.25 \pm 0.04$. If L1689 turns out to be representative, the large dispersion in polarization angle described above may arise from the high concentration of gas usually associated with a young cluster, rather than from the stars or their winds.

Indeed, if L1688 and L1689 are considered together as the massive central core of the Ophiuchus complex, and if L1709, L1712, and L1755 are considered together as the less massive filamentary outskirts of the complex, then the difference in polarization distributions is most dramatic, as illustrated in Figure 5*b*. There the central core has $s = 0.6 \pm 0.1$ for 61 points, while the filaments have $s = 0.22 \pm 0.01$ for 88 points. The mean polarization angles are also shifted: the central core has $\bar{\Theta}_E = 44° \pm 5°$, while the filaments have $\bar{\Theta}_E = 57° \pm 1°$.

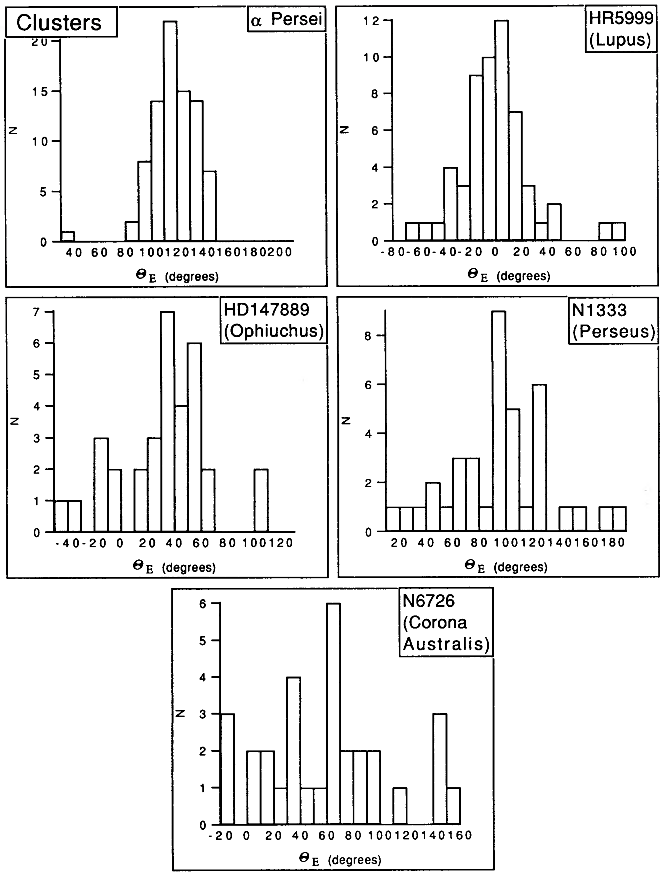

FIG. 3.—Number distributions of polarization angle for four embedded star clusters, and for one evolved cluster with low extinction (α Per), in order of increasing dispersion *s*.

2.5. *Polarization Distributions in Complexes*

Table 1C and Figure 4 show polarization information for six complexes. Each distribution is defined either by the polarization data within the boundaries specified in columns (2)–(5), in Tables 1A and 1B, or by the sum of the distributions for component clouds, already listed individually in Tables 1A and 1B.

The relation of the dispersion for a complex and the dispersions of its individual clouds can depend on sampling and data handling. If two cloud distributions have different dispersions, their sum can be narrow or broad, if the narrow distribution has significantly more or fewer data points than the broad distribution. If two cloud distributions have the same dispersion, their sum can again be narrow or broad, depending on the separation of their means and the relative number of points in each cloud distribution. To avoid bias, the surface density of data points within each part of a complex should be the same. Otherwise the width of the sum will be biased toward that of the component with the densest sampling. Other aspects of sampling are discussed in § 5.4.

Among the complexes considered here, all have reasonably uniform sampling within each of their component clouds, but some have variations in the sampling density and/or continuity of sampling from cloud to cloud. The Corona Australis complex has continuous sampling from the region designated here as NGC 6726 to the region designated GF 23, since each region is just a subdivision of the original, continuously sampled map of VCT. The Perseus complex also has continuous and uniform sampling, based on the large-scale map of Goodman et al. (1990). (The more densely sampled, small-scale map of the NGC 1333 region by Vrba et al. 1976 is not included in the complex data set [Fig. 4 and Table 1C], because of its greater sampling density. But the NGC 1333 map is used for the cluster data set [Fig. 3 and Table 1B], where the difference in sampling density is unimportant.) The Perseus distribution has some added uncertainty because of its editing, described in § 2.2.

Each of the Lupus and Chamaeleon complexes has about the same sampling density from one individual cloud to the next. But each complex also has at least one gap between its component clouds where no data were taken. For Chamaeleon this gap is probably unimportant, since the individual clouds have about the same mean and dispersion in polarization angle. For Lupus the gaps are probably important, since the mean polarization angle $\bar{\Theta}_E$ changes by 10° or more as one goes southward from Lupus 1 to 2, from 2 to 3, and from 3 and 4. For Taurus and Ophiuchus the maps used for the complex data set have gaps, and also clouds with abnormally dense sampling. However, the gap areas are relatively small, in contrast to those in Lupus and Chamaeleon, and the number of data points with dense sampling is probably too small to affect the overall distribution substantially.

These considerations of sampling suggest that the distributions for Corona Australis, Chamaeleon, Taurus, and Ophiuchus are fairly reliable, while those for Lupus and Perseus are less reliable.

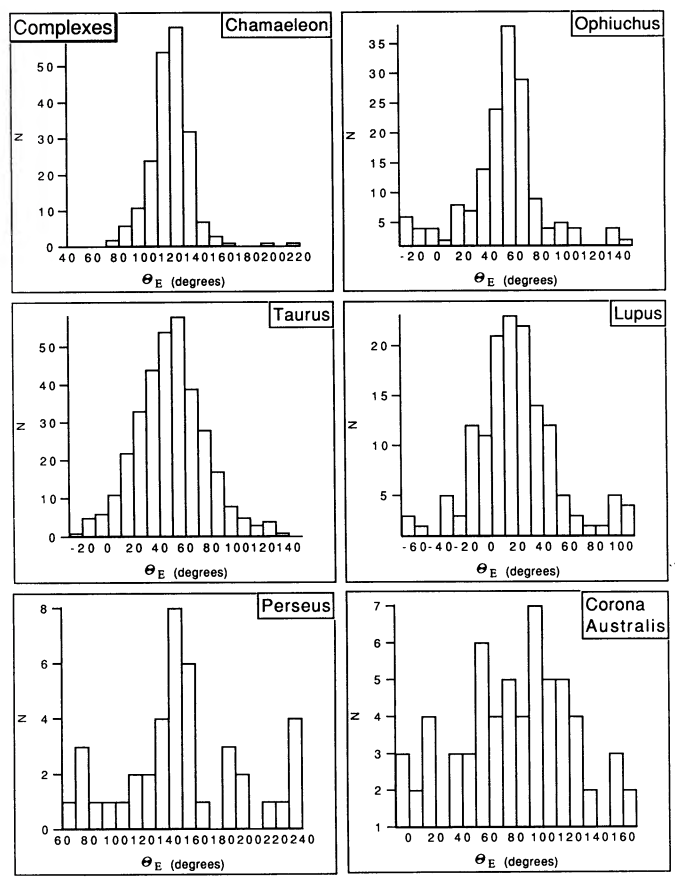

FIG. 4.—Number distributions of polarization angle for six dark cloud complexes, in order of increasing dispersion *s*.

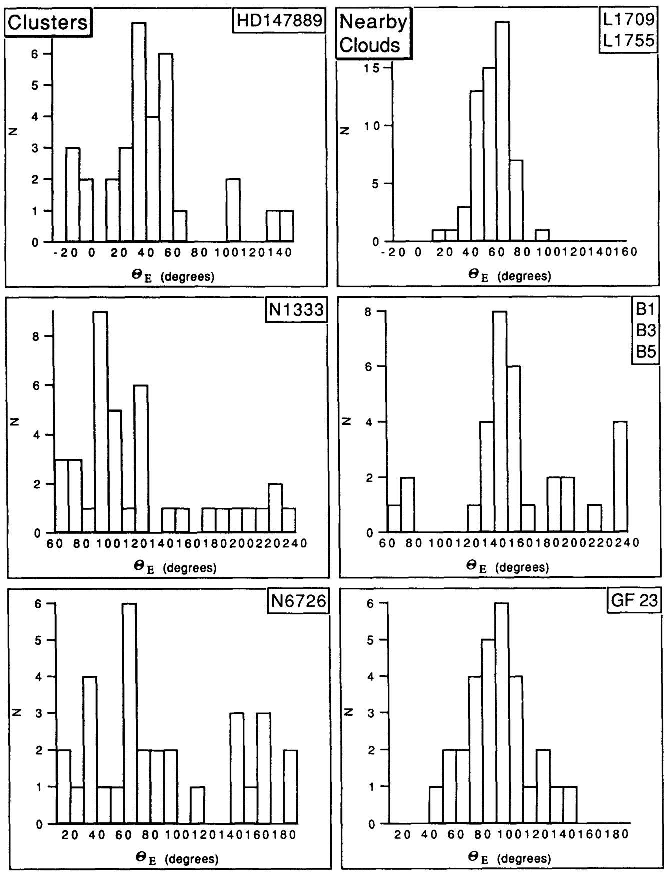

FIG. 5a

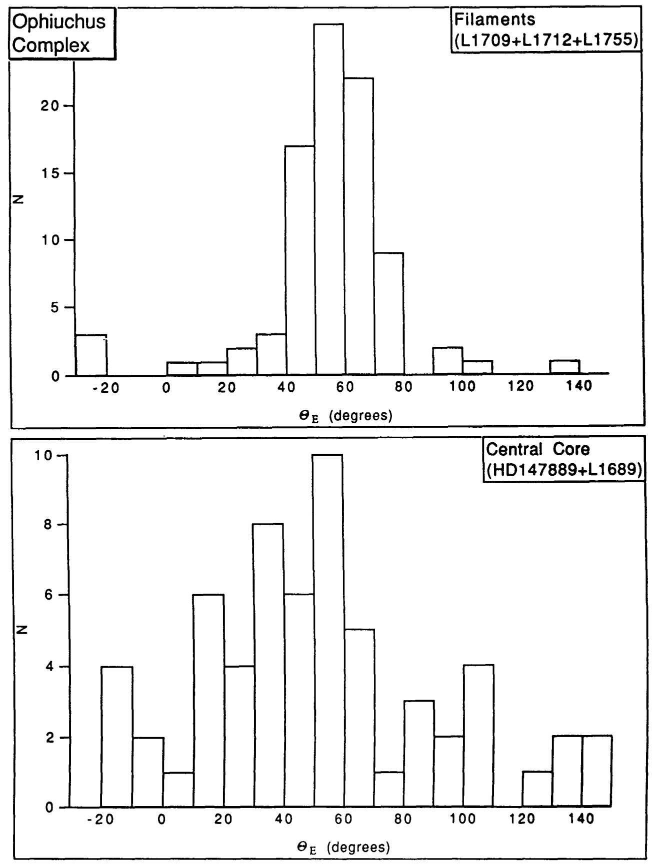

FIG. 5b

FIG. 5.—(*a*) Number distributions of polarization angle for three embedded star clusters (*left-hand panels*), and their neighboring dark clouds (*right-hand panels*). The cluster distributions are broader than the neighboring dark cloud distributions and have different means than do the neighboring dark cloud distributions. Each pair of distributions has a common scale of polarization angle. (*b*) Comparison of distributions for the Ophiuchus complex, combining L1688, which contains the HD 147889 cluster, with L1689 as the massive central core of the complex; and L1709, L1712, and L1755 as the less massive, filamentary extensions. The difference between the two polarization distributions is similar to that between pairs in (*a*), but is more pronounced.

After allowing for these uncertainties, the data for the complexes show that Chamaeleon is remarkably uniform in its polarization distribution, with dispersion s only 0.22. Taurus, like Chamaeleon, has no areas with enhanced dispersion, but unlike Chamaeleon it has zones with distinctly different means (or perhaps a systematic pattern of smoothly varying mean polarization). For Taurus, $s = 0.43$. Lupus, with $s = 0.47$, resembles Taurus in its zonal variation, but differs in the presence of a small cluster, HR 5999 in Lupus 3 (Schwartz 1977). Perseus, Ophiuchus, and Corona Australis have more substantial embedded star clusters than do Chamaeleon, Taurus, and Lupus. Their polarization distributions reflect the "competition" discussed above between their small-dispersion dark clouds and their larger-dispersion cluster regions. Thus the narrow distribution in Ophiuchus ($s = 0.34$) is dominated by the dark clouds, while that the Corona Australis ($s = 0.9$) is dominated by the cluster region.

3. MODELS OF THE DISTRIBUTION OF POLARIZATION DIRECTIONS

We have tried to make the simplest possible models that can reproduce the main feature of the number distributions in § 2, a single, symmetric local maximum. In § 3.1 we define and relate the angular positions of the magnetic field and the electric polarization in the plane of the sky. We present in § 3.2 the properties of the assumed uniform and nonuniform components of the magnetic field at any point in the model cloud, for nonuniform components whose directions have probabilities which are isotropic either in three dimensions or in the two dimensions perpendicular to the direction of the uniform component. In § 3.3. we describe the properties of the field components as viewed through N correlation lengths along the line of sight through the cloud. In § 3.4 we obtain the probability distribution of the position angle of optical polarization in terms of the uniform and nonuniform components to the line of sight. We discuss the properties of these distributions and several simple limiting cases.

3.1. *Magnetic Field Angles and Electric Polarization Angles*

We denote the direction of the magnetic field in the plane of the sky by Θ_B, measured counterclockwise from north over the range 0–2π. The corresponding direction of electric field polarization Θ_E has ambiguous sign, but by convention the direction that lies in the range 0–π is specified as the direction of polarization:

$$\Theta_E = \Theta_B , \qquad 0 \le \Theta_B < \pi , \tag{1a}$$

$$\Theta_E = \Theta_B - \pi , \quad \pi \le \Theta_B < 2\pi . \tag{1b}$$

We denote the mean value of Θ_B over all points in a cloud by $\bar{\Theta}_B$, and the corresponding mean direction of electric polarization by $\bar{\Theta}_E$. These angles $\bar{\Theta}_E$ and $\bar{\Theta}_B$ are related in the same way as are Θ_E and Θ_B in equations (1a) and (1b). We define the directions relative to the mean by

$$\theta_B = \Theta_B - \bar{\Theta}_B + 2\pi\ , \quad -2\pi \le \Theta_B - \bar{\Theta}_B < -\pi\ , \qquad (2a)$$

$$\theta_B = \Theta_B - \bar{\Theta}_B\ , \quad -\pi \le \Theta_B - \bar{\Theta}_B < \pi\ , \qquad (2b)$$

$$\theta_B = \Theta_B - \bar{\Theta}_B - 2\pi\ , \quad \pi \le \Theta_B - \bar{\Theta}_B \le 2\pi\ , \qquad (2c)$$

so that $-\pi \le \theta_B < \pi$, and by

$$\theta_E = \Theta_E - \bar{\Theta}_E + \pi\ , \quad -\pi \le \Theta_E - \bar{\Theta}_E < -\pi/2\ , \qquad (3a)$$

$$\theta_E = \Theta_E - \bar{\Theta}_E\ , \quad -\pi/2 \le \Theta_E - \bar{\Theta}_E < \pi/2\ , \qquad (3b)$$

$$\theta_E = \Theta_E - \bar{\Theta}_E - \pi\ , \quad \pi/2 \le \Theta_E - \bar{\Theta}_E \le \pi\ , \qquad (3c)$$

so that $-\pi/2 \le \theta_E < \pi/2$. Consequently,

$$\theta_E = \theta_B + \pi\ , \quad -\pi \le \theta_B < -\pi/2\ , \qquad (4a)$$

$$\theta_E = \theta_B\ , \quad -\pi/2 \le \theta_B < \pi/2\ , \qquad (4b)$$

$$\theta_E = \theta_B - \pi\ , \quad \pi/2 \le \theta_B \le \pi\ . \qquad (4c)$$

3.2. *Uniform and Nonuniform Field Components*

We assume a right-handed coordinate system as in Figure 6, where the x-axis points along $\bar{\Theta}_B$ and the z-axis points along the line of sight, in the same direction as the mean line-of-sight component of the magnetic field in the region of interest. These definitions are made for convenience, so that the mean plane-of-the-sky and line-of-sight components of the magnetic field always have positive sign.[1] Then

$$\tan\theta_B = \frac{B_y}{B_x}\ . \qquad (5)$$

The field is assumed to have a component that is uniform over the region of interst

$$\boldsymbol{B}_0 = \hat{x}B_{0x} + \hat{z}B_{0z}\ , \qquad (6)$$

where by definition $B_{0y} = 0$, and where the inclination i between B_0 and the line of sight is given by

$$\tan i = \frac{B_{0x}}{B_{0z}}\ . \qquad (7)$$

The field also has a nonuniform component

$$\boldsymbol{B}_n = \hat{x}B_{nx} + \hat{y}B_{ny} + \hat{z}B_{nz}\ , \qquad (8)$$

to be described by a probability distribution. The total field at any point in the cloud is then

$$\boldsymbol{B} = \boldsymbol{B}_0 + \boldsymbol{B}_n\ . \qquad (9)$$

The plane-of-the-sky fields are given by

$$\boldsymbol{B}_{xy} = \hat{x}B_x + \hat{y}B_y\ , \qquad (10)$$

$$\boldsymbol{B}_{nxy} = \hat{x}B_{nx} + \hat{y}B_{ny}\ , \qquad (11)$$

where

$$B_x = B_{0x} + B_{nx} \qquad (12)$$

and

$$B_y = B_{ny}\ . \qquad (13)$$

We let the nonuniform component $\boldsymbol{B}_n$ obey one of two probability distributions. In the three-dimensional case, all of the three space components of $\boldsymbol{B}_n$ are Gaussian random variables, with identical probability density

$$f_u(u) = \frac{1}{(2\pi)^{1/2}\sigma_B}\exp\left(-\frac{u^2}{2\sigma_B^2}\right)\ , \qquad (14)$$

where u represents each of B_{nx}, B_{ny}, and B_{nz}. On the plane of the sky, the contour of constant probability that B_{nxy} has a particular value is a circle. This three-dimensional case is meant to simulate an isotropic "turbulent" field, or a super-

[1] The sign convention adopted here for the line-of-sight component of the magnetic field is not the same as that generally used for Zeeman observations, in which a positive (negative) sign indicates a field directed away from (toward) the observer.

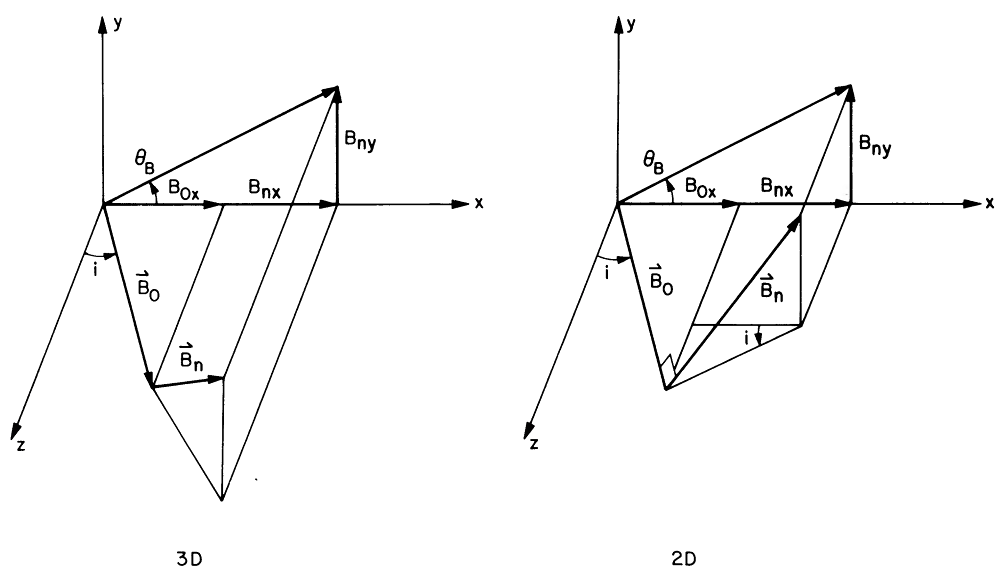

FIG. 6.—Geometrical relations among magnetic field vectors in the two-dimensional and three-dimensional models

position of hydromagnetic waves propagating in many directions.

In the two-dimensional case, $\boldsymbol{B}_n$ has two orthogonal components B'_{ny} and B'_{nz}, each a Gaussian random variable in the plane perpendicular to $\boldsymbol{B}_0$, following equation (14), where u represents each of B'_{ny} and B'_{nz}, and where

$$B'_{ny} = B_{ny} , \tag{15a}$$

$$B'_{nz} = \frac{B_{nx}}{\cos i} . \tag{15b}$$

On the plane of the sky the contour of constant probability that B_{nxy} has a particular value is now an ellipse with major axis in the y-direction. The relative size of the minor axis depends on the inclination i of the uniform component B_0 to the line of sight: when $i = 0$, $B_{0x} = 0$, and the ellipse is a circle. When $i = \pi/2$, $B_{0x} = B_0$, and the ellipse is a line in the y-direction. This two-dimensional case is meant to simulate simple transverse hydromagnetic waves propagating along the direction of $\boldsymbol{B}_0$.

A model with both uniform and nonuniform components could be even simpler than those given above, by restricting the amplitude of the nonuniform component to a single value of B_n, rather than a distribution of possible values. However, the resulting probability density of polarization angle is then bimodal, with peaks at $\pm\arcsin(B_n/B_0)$. This distribution does not resemble the typical observed distribution, so we do not consider it further.

Figure 6 illustrates the geometrical relationships among the variables in the two- and three-dimensional cases. There $\boldsymbol{B}_0$ and the plane-of-the-sky vectors are the same from case to case, but the line-of-sight components necessarily differ.

3.3. *Line-of-Sight–Averaged Field Components*

The magnetic field responsible for the polarization angle observed in a particular direction is not generally the field, discussed above, at a single point along the line of sight. Rather it is the average of the various field vectors encountered by the beam of starlight as it traverses the cloud, weighted by the specific extinction in each segment of path (e.g., Jones 1989). To account for this, we assume that the nonuniform component of the field can be described by a "correlation length" l. Thus, values of B_n at two three-dimensional positions in a cloud separated by less than l are correlated, and nearly equal, while values of B_n at two positions separated by more than l are independent, and can differ greatly, each subject to the probability distributions represented by equation (14).

If each correlation length along the line of sight has the same optical depth (<1) to the incident radiation, then the contribution of the nonuniform component to the total field responsible for the observed polarization is the mean of the N independent samples of the nonuniform field along the line of sight. The probability that this mean field has a particular value is given by equation (14) with σ_B replaced by $\sigma_B/N^{1/2}$, or

$$g_u(u) = \frac{N^{1/2}}{(2\pi)^{1/2}\sigma_B} \exp\left(-\frac{Nu^2}{2\sigma_B^2}\right) , \tag{16}$$

where u is now the mean of N independent samples of each of B_{nx}, B_{ny}, and B_{nz} in the three-dimensional case, or of each of B'_{ny} and B'_{nz} in the two-dimensional case.

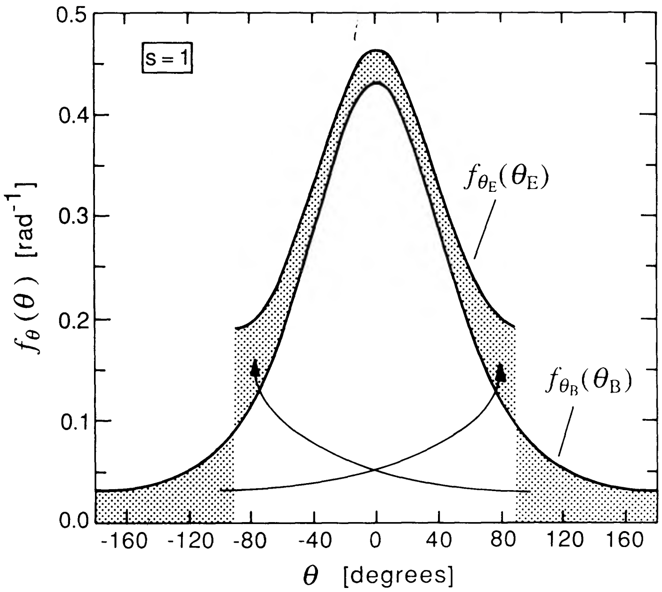

FIG. 7.—Relations between the probability density $f_{\theta_B}(\theta_B)$ for the magnetic field direction and $f_{\theta_E}(\theta_E)$ for the electric polarization direction.

The value of N typical for most observations of polarization probably lies in the range 1–10, as discussed in § 4.2.

3.4. *Model Probability Distributions of Polarization Angle*

We denote the probability density with respect to the observed relative polarization angle θ_E, and with argument θ_E, as $f_{\theta_E}(\theta_E)$. To find $f_{\theta_E}(\theta_E)$, we first obtain $f_{\theta_B}(\theta_B)$ using standard methods of probability theory (e.g., Papoulis 1965; Davenport & Root 1958). For the three-dimensional case, this calculation is well known in radio interferometry: $f_{\theta_B}(\theta_B)$ is formally identical to the probability that the interferometer phase has a particular value in the presence of Gaussian random noise (Thompson, Moran, & Swenson 1986, hereafter TMS, eq. [6-56b]). Thus, our variable θ_B corresponds to TMS's variable ϕ, and our parameter s (defined in eq. [19]) corresponds to TMS's parameter $\sigma/|\mathscr{V}|$.

From $f_{\theta_B}(\theta_B)$ we obtain $f_{\theta_E}(\theta_E)$ using equations (4a)–(4c):

$$f_{\theta_E}(\theta_E) = \begin{cases} f_{\theta_B}(\theta_E) + f_{\theta_B}(\theta_E + \pi) , & -\frac{\pi}{2} \le \theta_E < 0 , \quad (17a) \\ f_{\theta_B}(\theta_E) + f_{\theta_B}(\theta_E - \pi) , & 0 \le \theta_E < \frac{\pi}{2} . \quad (17b) \end{cases}$$

This transformation is illustrated in Figure 7 for $s = 1$.

Henceforth in this paper, f will always indicate a probability density with respect to θ_E, and with argument θ_E. Subscripts and superscripts on f will be descriptive labels; symbols in parentheses will be parameters.

The resulting expression can be written for the three-dimensional case, for the entire range $-\pi/2 \le \theta_E < \pi/2$, as

$$f^{3D} = \frac{1}{\pi} \exp\left(-\frac{1}{2s^2}\right) + \frac{\cos\theta_E}{(2\pi)^{1/2}s} \times \exp\left[-\frac{1}{2}\left(\frac{\sin\theta_E}{s}\right)^2\right] \operatorname{erf}\left(\frac{\cos\theta_E}{2^{1/2}s}\right) , \tag{18}$$

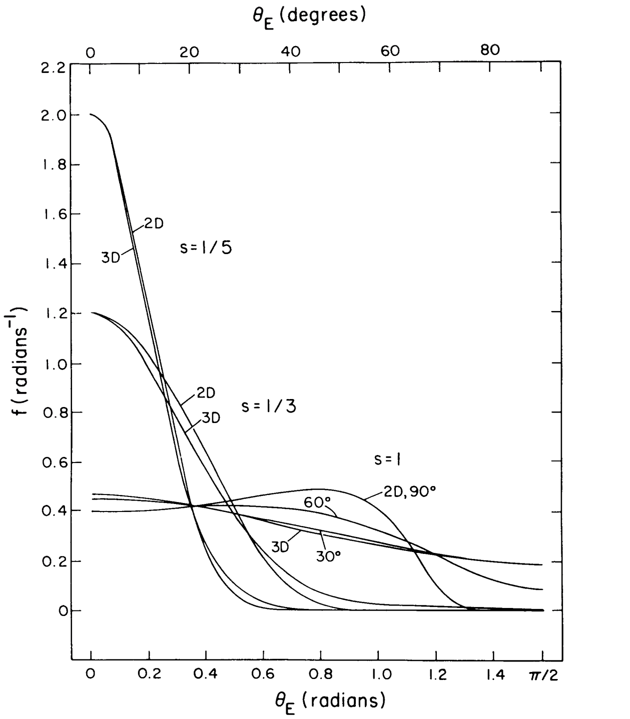

FIG. 8.—Curves of f^{3D} and f^{2D} vs. θ_E as in eqs. (18) and (20), for values of the parameter $s = \frac{1}{5}, \frac{1}{3}$, and 1. For $s = 1$, f^{2D} is shown for inclination 30°, 60°, and 90° between the uniform magnetic field and the line of sight. For $s = \frac{1}{5}$ and $\frac{1}{3}$, f^{2D} is shown for $i = 90°$ only.

where[2]

$$s = \frac{\sigma_B}{N^{1/2} B_{0x}} , \tag{19}$$

and the probability density is independent of inclination i. For the two-dimensional case,

$$f^{2D} = \alpha^2 \left\{ \frac{c}{\pi} \exp\left[\frac{-1}{2(cs)^2}\right] + \frac{\alpha \cos \theta_E}{(2\pi)^{1/2} s} \times \exp\left[-\frac{1}{2}\left(\frac{\alpha \sin \theta_E}{s}\right)^2\right] \operatorname{erf}\left[\frac{\alpha \cos \theta_E}{2^{1/2} cs}\right] \right\} , \tag{20}$$

where

$$\alpha^{-2} = \cos^2 \theta_E + c^2 \sin^2 \theta_E \tag{21a}$$

and

$$c = \cos i . \tag{21b}$$

Figure 8 shows curves of f^{3D} and f^{2D} for $s^{-1} = 1$, 3, and 5. For $s^{-1} = 1$, f^{2D} is shown for inclinations $i = 30°$, 60°, and 90°. For $s^{-1} = 3$ and 5, f^{2D} is shown only for $i = 90°$, since that curve differs only slightly from those for smaller inclinations.

The main features of the probability function f^{2D} and f^{3D} are the following:

1. For $s \ll 1$, f^{2D} and f^{3D} are nearly equal, independent of inclination i, and can be approximated by

$$f_{s \ll 1} = \frac{1}{(2\pi)^{1/2} s} \exp\left(-\frac{\theta_E^2}{2s^2}\right) , \tag{22}$$

which follows from equations (18) and (20) by using the small-angle approximation, and by approximating erf x by 1 for $x \gg 1$. Equation (22) is convenient, since it is a Gaussian with dispersion s radians. If $f_{s \ll 1}$ gives a good fit to an observed distribution of polarization direction, which has rms dispersion σ_{θ_E}, then

$$\sigma_{\theta_E} \simeq \frac{\sigma_B}{N^{1/2} B_{0x}} = s , \tag{23}$$

in accord with the estimate of Jokipii & Parker (1969) when $N = 1$.

2. As s approaches unity, f^{2D} and f^{3D} become broader; they begin to differ significantly from each other: f^{3D} can still be approximated by a Gaussian, while f^{2D} is more nearly rectangular.

3. For s near unity, f^{2D} depends significantly on inclination i. Its limiting cases can be written

$$f^{2D}(i = 0) = \frac{1}{\pi} , \tag{24a}$$

$$f^{2D}\left(i = \frac{\pi}{2}\right) = \frac{\exp\{-(1/2)[(\tan \theta_E)/s]^2\}}{(2\pi)^{1/2} \cos^2(\theta_E)} . \tag{24b}$$

For $i = 0$ (eq. [24a]), f^{2D} is flat, since the plane-of-the-sky component of the uniform field, B_{0x}, equals zero, and since the plane-of-the-sky component of the nonuniform field has equal probability of pointing in any direction. For $i = \pi/2$ (eq. [24b]) and $s \simeq 1$, f^{2D} has a weak local minimum at $\theta_E = 0$, in contrast to the local maximum in f^{3D} at $\theta_E = 0$.

4. For all s, f^{3D} is well approximated by a Gaussian with dispersion s, normalized over $-\pi/2 \le \theta_E \le \pi/2$, given by

$$g_0 = \frac{\exp(-\theta_E^2/2s^2)}{(2\pi)^{1/2} s \operatorname{erf}(\pi/2^{3/2} s)} . \tag{25}$$

When $s \ll 1$, equation (25) reduces to equation (22), as expected. Another good approximation to f^{3D} is g_1, a best-fit Gaussian with both dispersion and amplitude as free parameters, although this function is not necessarily properly normalized. Figure 9 shows f^{3D}, g_0, and g_1 versus θ_E, for $s = \frac{1}{5}, \frac{1}{3}$, 1, and 2. The three functions are extremely similar for all θ_E when $s < 1$, as implied by equation (22). They also agree closely enough for most purposes when $s \gtrsim 1$. It may be more convenient to use g_0 or g_1 than f^{3D} for numerical fitting and calculation.

4. APPLICATION OF THE MODELS TO OBSERVATIONS

4.1. *Estimation of s*

To estimate the dispersion of polarization angle s, each distribution in Figures 2, 3, and 4 was divided by $N_{tot} \Delta\Phi$. Here N_{tot} is the total number of points in the distribution, given in Table 1, and $\Delta\Theta$ is the bin width, equal to 10°, or $\pi/18$ radians. This normalization yields the observed probability distribution f_{obs}. We fit this distribution with the function f^{3D} given in equation (18). When written in terms of Θ_E, using equation (3), f^{3D} depends only on the variable Θ_E and on the parameters $\bar{\Theta}_E$ and s. The values of $\bar{\Theta}_E$ and s, and their 1 σ uncertainties, were obtained from a nonlinear least-squares fitting program. These four values are given in Table 1.

Figure 10 shows the fit of f^{3D} and of g_1, a Gaussian with free amplitude, center, and dispersion, to the distribution for the Taurus complex, for which there are 339 data points, the largest number of points among the regions considered in this

[2] Note that the error function in eq. (18) is based on the "standard" definition, as given, e.g., in Abramowitz & Stegun (1985), and not on the definition used by Papoulis (1965).

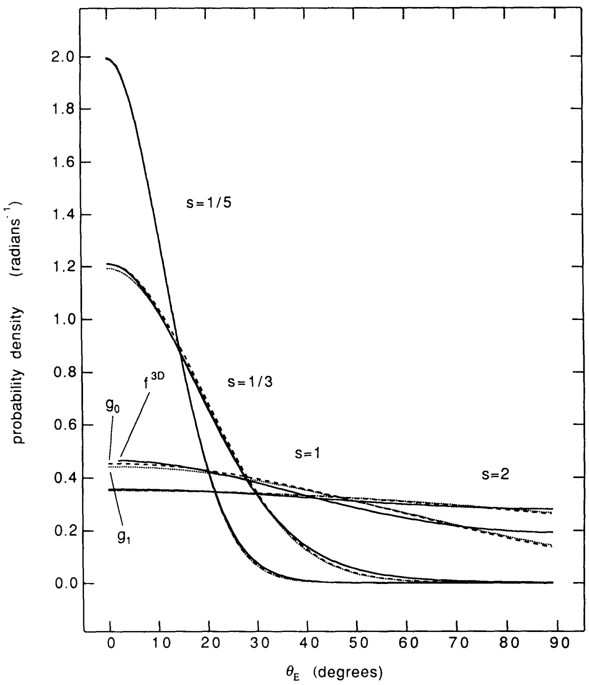

FIG. 9.—*Solid line*: curves of f^{3D} as in eq. (18), with parameter $s = \frac{1}{5}$, with parameter $s = \frac{1}{5}, \frac{1}{3}$, 1, and 2; *dashed line*: g_0 as in eq. (25), a normalized Gaussian with dispersion s; *dotted line*: g_1, a Gaussian with free amplitude and dispersion that best fits f^{3D}.

paper. For this distribution, $s = 0.43 \pm 0.01$. The functions are extremely similar to each other, and each provides an excellent fit to the data.

We used f^{3D} rather than f^{2D} for fitting because for small s the two functions are indistinguishable, as discussed in § 3.4,

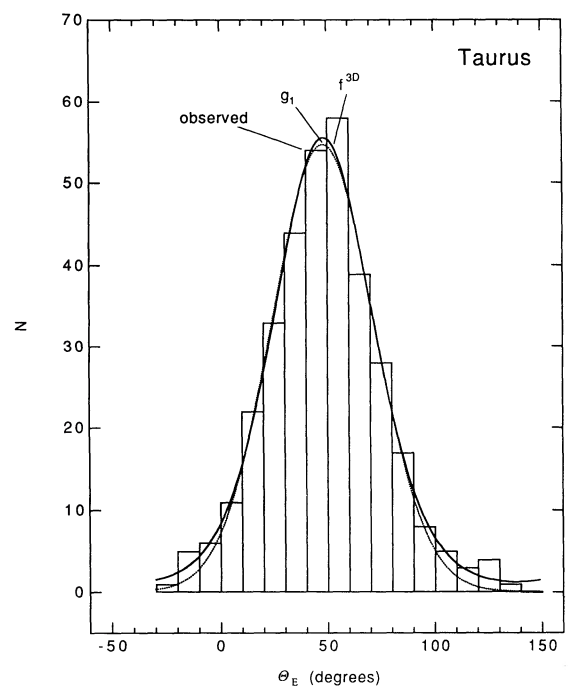

FIG. 10.—*Histogram*: observed number distribution of polarization angle for a Taurus complex; *solid line*: best fit of f^{3D}; *dotted line*: best fit of g_1, a Gaussian with free amplitude, center, and dispersion.

and because for large s the observed distribution tends to have a central maximum, as does f^{3D}, rather than a plateau with a central minimum, as does f^{2D}.

4.2. *Estimation of N*

The number N of magnetic field correlation lengths along the line of sight through a cloud should be evident as a size scale within which the polarization directions have relatively small dispersion, but beyond which they have larger dispersion.

Some of the optical polarization maps summarized in Table 1 show evidence for this property. Five of the 15 clouds without clusters in Table 1A have "spatial pattern type" 3, indicating at least two spatial zones within which a mean direction is clearly evident, and between which a difference in mean direction is also evident. Three additional clouds have type 2 or type 4, indicating two well-defined directions in the same zone, or one well-defined direction and one poorly defined direction in neighboring zones. The Taurus complex has more than five regions with distinctly different position angles, each separated from the next by a few parsecs (e.g., Tamura et al. 1988; Scalo 1990). This evidence for variation in position angle across the line of sight suggests that at least some clouds have similar variation in position angle along the line of sight.

If the nonuniform component arises from hydromagnetic waves, then an upper limit on N can be crudely estimated from the cutoff wavelength $\lambda_{\rm min}$, the shortest wavelength for which Alfvén waves can propagate in a region. Alfvén waves of wavelength shorter than $\lambda_{\rm min}$ cannot propagate because the ions do not have enough time in a wave period to couple their wave energy to the neutrals by collisions (e.g., Mouschovias 1987). The wavelength λ corresponds approximately to a correlation length: two samples of the field, with separation much smaller than λ, will be highly correlated, since the samples will have a small phase difference. Conversely, two samples of the field, with separation much larger than λ, will be uncorrelated, since these samples can have any phase difference. In a region with a spectrum of wavelengths, the effective correlation length will be a weighted average over the allowed range of wavelengths. Thus $\lambda_{\rm min}$ represents the smallest possible correlation length.

The number of such lengths in a region with line-of-sight extent L is then

$$N_{\rm max} = \frac{L}{\lambda_{\rm min}} = \frac{L}{\pi v_{\rm A} \tau_{\rm ni}}\,, \qquad (26)$$

where $v_{\rm A}$ is the Alfvén speed in the region and $\tau_{\rm ni}$ is the ion-neutral collision time (Shu, Adams, & Lizano 1987; Mouschovias 1987). Equation (26) can be written

$$N_{\rm max} = 3C\gamma\left(\frac{m}{\pi^{1/2}}\right)\frac{\mathcal{N}}{B}\,, \qquad (27)$$

where C is the coefficient of ionization equilibrium, 3×10^{-16} cm$^{-3/2}$ $g^{1/2}$; γ is the drag coefficient associated with momentum exchange in ion-neutral collisions, 3.5×10^{13} cm^3 g^{-1} s^{-1} (Shu, Adams, & Lizano 1987); $\mathcal{N}$ is the mean column density through a uniform sphere; and B is the field strength. Employing the usual gas-to-dust relation $\mathcal{N}/A_V = 1 \times 10^{21}$ cm^{-2} mag^{-1}, where A_V is the visual extinction, we write equation (27) in practical units as

$$N_{\rm max} = 69\left(\frac{A_V}{\rm mag}\right)\left(\frac{B}{\mu{\rm G}}\right)^{-1}\,. \qquad (28)$$

The typical dark cloud environment observed with optical polarimetry has $A_V \simeq 1$ mag, and measurements of the Zeeman effect suggest $B = 5$–10 μG (Heiles 1988), yielding $N_{\max} \simeq$ 7–14.

A similar estimate follows from assuming that the magnetic and gravitational energy densities are equal, whence $A_V/B \simeq 0.17$ mag μG^{-1}, a constant (Chandrasekhar & Fermi 1953; Elmegreen 1978; Myers & Goodman 1988b). Then equation (28) implies $N_{\max} \simeq 12$, also a constant. This last estimate is dimensionally equivalent to the well-known ratio of ambipolar diffusion and free-fall time scales (e.g., Shu, Adams, & Lizano 1987).

4.3. *Estimation of the Magnitude and Direction of the Magnetic Field*

When several spatially independent observations of the Zeeman shift have been made in a region, a map of the line-of-sight magnetic field B_z can be constructed. If the map samples the same volume as a polarization map of the plane-of-sky field direction, and if each set of map data has a number distribution with a single maximum, the models of § 3 allow the three-dimensional field to be estimated.

The mean $\bar{B}_z$ and dispersion σ_{B_z} of the Zeeman data are related to the models of § 3 by

$$B_{0z} = \bar{B}_z \, , \tag{29}$$

$$\frac{\sigma_B}{N^{1/2}} = \begin{cases} \sigma_{B_z} \, , & D = 3 \, , \quad (30a) \\ \dfrac{\sigma_{B_z}}{\sin i} \, , & D = 2 \, , \quad (30b) \end{cases}$$

where D is the number of dimensions in the nonuniform component. From equations (7) and (19),

$$\frac{\sigma_B}{N^{1/2}} = B_{0z} s \tan i \, . \tag{31}$$

Eliminating $\sigma_B/N^{1/2}$ from equations (30) and (31),

$$i = \arctan 2w \, , \qquad D = 3 \, , \tag{32a}$$

$$i = \arccos \left[(w^2 + 1)^{1/2} - w\right] \, , \quad D = 2 \, , \tag{32b}$$

where

$$w = \frac{\sigma_{B_z}}{2 \, s \, B_{0z}} \, . \tag{33}$$

The orientation of $\boldsymbol{B}_0$ inferred from the observations has two possible values, because the position angle Θ_B of the magnetic field in the plane of the sky is related to the observed electric polarization angle Θ_E either by $\Theta_B = \Theta_E$ or by $\Theta_B = \Theta_E + \pi$, as described in § 3.1. Thus, from equations (1), (6), and (7),

$$\hat{\boldsymbol{B}}_0 = (\hat{\boldsymbol{N}} \cos \Theta_B + \hat{\boldsymbol{E}} \sin \Theta_B) \sin i + \hat{z} \cos i \, . \tag{34}$$

So either

$$\hat{\boldsymbol{B}}_0 = (\hat{\boldsymbol{N}} \cos \Theta_E + \hat{\boldsymbol{E}} \sin \Theta_E) \sin i + \hat{z} \cos i \, , \tag{35a}$$

when $\Theta_B = \Theta_E$, or

$$\hat{\boldsymbol{B}}_0 = -(\hat{\boldsymbol{N}} \cos \Theta_E + \hat{\boldsymbol{E}} \sin \Theta_E) \sin i + \hat{z} \cos i \, , \tag{35b}$$

when $\Theta_B = \Theta_E + \pi$. Here $\hat{\boldsymbol{B}}_0$, $\hat{\boldsymbol{N}}$, and $\hat{\boldsymbol{E}}$ are unit vectors in the directions of $\boldsymbol{B}_0$, north, and east, respectively. These relations are illustrated in Figure 11.

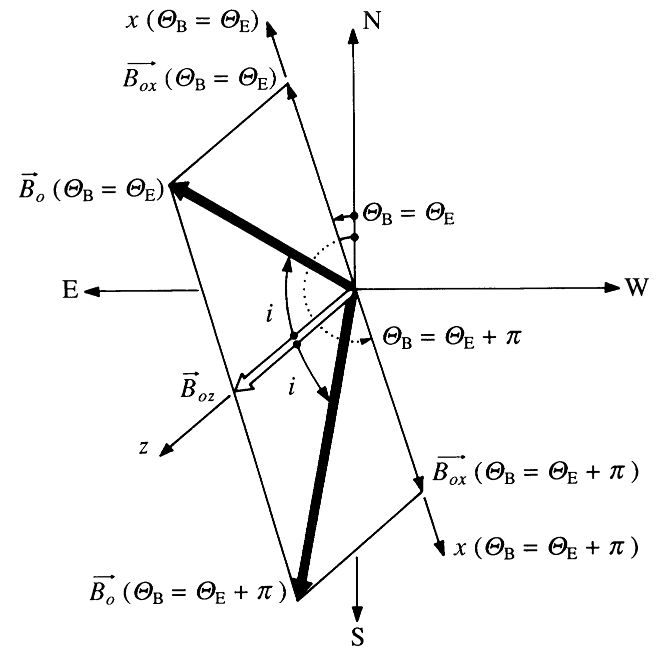

FIG. 11.—Diagram showing ambiguity in direction of the three-dimensional uniform component $\boldsymbol{B}_0$ of the magnetic field, deduced from observations of optical polarization angle Θ_E and of the Zeeman effect. The two possible directions of $\boldsymbol{B}_0$ arise from the two possible directions of the plane-of-the-sky component $\boldsymbol{B}_{0x}$, i.e., either $\Theta_B = \Theta_E$ or $\Theta_B = \Theta_E + \pi$. Each vector is labeled by the symbol closest to its arrowhead.

Once i is known from equation (32), the magnitude of the uniform field is obtained from

$$B_0 = \frac{B_{0z}}{\cos i} \, . \tag{36}$$

The rms field, including both uniform and nonuniform components, is then

$$\langle B^2 \rangle^{1/2} = (B_0^2 + D\sigma_B^2)^{1/2} \, , \tag{37}$$

and the ratio of nonuniform and uniform energy densities is

$$\frac{\mathbf{M}_n}{\mathbf{M}_u} = \frac{D\sigma_B^2}{B_0^2} \, . \tag{38}$$

The foregoing equations needed to compute i, B_0, $\langle B^2 \rangle^{1/2}$, and $\mathbf{M}_n/\mathbf{M}_u$ are summarized in Table 2. To use Table 2, one evaluates the equations in order from left to right.

The expressions in Table 2 differ slightly for the three-dimensional and two-dimensional models. If the parameter s deduced from the optical polarization data differs significantly between the three-dimensional and two-dimensional cases, as when $s \gtrsim 1$ or when the FWHM of the position angle distribution exceeds about 100°, then the deduced position angle can differ by more than 15°. Otherwise, the deduced position angles differ by less than 15°. For most polarization data currently available, $s \leq 1$, so that the quantities in Table 2 do not generally allow one to distinguish between three-dimensional and two-dimensional cases. The few distributions with $s \simeq 1$ in the sample considered here resemble f^{3D} more closely than the f^{2D} cases with $i \gtrsim 60°$. But if $i < 60°$, the data do not allow us to distinguish between f^{2D} and f^{3D}.

The quantities σ_B, $\langle B^2 \rangle^{1/2}$, and $\mathbf{M}_n/\mathbf{M}_u$ depend on N, the number of correlation lengths of the nonuniform component

TABLE 2

MAGNETIC PROPERTIES DERIVABLE FROM MAPS OF POLARIZATION DIRECTION AND OF THE ZEEMAN SHIFT

Model	i	B_0	σ_B	$\langle B^2 \rangle^{1/2}$	$\mathbf{M}_n/\mathbf{M}_u$
Three-dimensional	arctan $2w$	$B_{0z}/\cos i$	$N^{1/2}\sigma_{B_z}$	$(B_0^2 + 3\sigma_B^2)^{1/2}$	$3\sigma_B^2/B_0^2$
Two-dimensional	arccos $[(w^2 + 1)^{1/2} - w]$	$B_{0z}/\cos i$	$N^{1/2}\sigma_{B_z}/\sin i$	$(B_0^2 + 2\sigma_B^2)^{1/2}$	$2\sigma_B^2/B_0^2$

NOTE.—B_0 is the magnitude of the uniform component of the field, inclined at an angle i to the line of sight; σ_B is the dispersion of the nonuniform component, isotropic either in three dimensions or in the two dimensions perpendicular to the direction of $\boldsymbol{B}_0$. N is the number of correlation lengths of the nonuniform component along the line of sight. $\langle B^2 \rangle^{1/2}$ is the rms field strength. B_{0z} is the mean over the map of the field strength B_z deduced from Zeeman observations, and σ_{B_z} is the dispersion of B_z about its mean; $w = \sigma_{B_z}/2B_{0z}s$, where s is deduced from the polarization map as in § 3. $\mathbf{M}_n/\mathbf{M}_u$ is the ratio of magnetic energy densities in the nonuniform and uniform components. See also eqs. (29)–(38).

along the line of sight. As discussed above, N probably lies in the range 1–10 for many of the clouds considered here.

4.4. *An Example: L204*

In the dark cloud Lynds 204 (L204), Heiles (1988) has made H I Zeeman measurements on a grid of 27 positions covering approximately a 6×15 pc area, and McCutcheon et al. (1986) have made well-sampled optical polarization measurements covering a similar region.

Using the 49 polarization measurements of McCutcheon et al. summarized in Table 1, we find $\bar{\Theta}_E = 71°$ and $s = 0.40$, corresponding to $\sigma_{\theta_E} = 25°$, in the Gaussian approximation (eq. [18]).

The H I spectra in L204 are best fitted by a two-component model, comprising a wide emission profile plus a narrower self-absorption feature. Thus, B_{0z} and σ_{B_z} can be extracted from the Zeeman data in two ways—using the distribution of either the 27 line-of-sight field strength values derived from the wide H I emission profiles or the 12 field values based on the absorption features. Since the optical polarization measurements sample mostly the $A_V \lesssim 1$ gas, and the H I self-absorption is likely produced at slightly greater column densities, it is probably more appropriate to use the emission measurements. However, if the distribution of uniform and nonuniform field derived from the polarization data is also representative of the denser gas in L204, then the case can be made for using the self-absorption Zeeman values.

In Table 3 we present the results of applying the formulae in Table 2 to L204, under the assumptions $N = 1$ and $N = 10$. We list only the results for the three-dimensional case, since the results for the two-dimensional case are not significantly different, owing to the small value of s in L204. In order for the nonuniform and uniform field energies to be equal in L204, $N \approx 3$ using the absorption measurements, and $N \approx 4$ using the emission measurements.

Using equation (35), the total uniform field, $\boldsymbol{B}_0$, in L204 can be written

$$\boldsymbol{B}_0 = 6.2\ \mu\mathrm{G}[\pm(0.24\hat{\boldsymbol{N}} + 0.69\hat{\boldsymbol{E}}) + 0.68\hat{\boldsymbol{z}}]\ , \tag{39a}$$

using the Zeeman measurements for H I emission, or

$$\boldsymbol{B}_0 = 12.9\ \mu\mathrm{G}[\pm(0.29\hat{\boldsymbol{N}} + 0.83\hat{\boldsymbol{E}}) + 0.49\hat{\boldsymbol{z}}]\ , \tag{39b}$$

using the Zeeman measurements for H I self-absorption. In either case, the z-axis points in the direction of the measured line-of-sight component, or for L204 away from the observer.

5. DISCUSSION

5.1. *Regions of Large and Small Dispersion*

The data in § 2 indicate that the average embedded cluster has substantially broader dispersion in polarization angle, $s = 0.4$–0.5, than does the average cloud with more modest star formation, $s = 0.2$–0.3. The embedded cluster also has broader dispersion than its neighboring dark cloud, and its mean polarization angle is substantially shifted from that of the cloud. A less certain conclusion, based on comparison of the star-rich and star-poor clouds L1688 and L1689, is that the enhanced polarization dispersion is tied more closely to the dense gas associated with the cluster than to winds and other consequences of the recently formed stars.

One can understand this behavior in a simple picture where the embedded cluster tends to form near a center of gravity of the molecular cloud complex. There the concentration of mass, and the rate of mass accumulation, are most likely to be higher than in other parts of the complex. In this location, gravitational forces have evidently prevailed to some degree over magnetic and kinetic pressures tending to resist infall. Thus, over the duration of the accumulation, the infall speed has on average exceeded the Alfvén speed. But it is also likely that the accumulating gas has sufficient ionization to couple to the associated field, so that accumulating matter carries its magnetic field lines inward. This process will tend to increase the

TABLE 3

MAGNETIC PROPERTIES DERIVED FOR L204

Line Type	B_{0z} (μG)	σ_{B_z} (μG)	w	i	B_{0x} (μG)	B_0 (μG)	N	σ_B (μG)	$\langle B^2 \rangle^{1/2}$ (μG)	$\mathbf{M}_n/\mathbf{M}_u$
Emission	4.2	1.8	0.54	47°	4.5	6.2	1	1.8	6.9	0.26
							10	5.7	23	2.6
Absorption	6.4	4.5	0.88	60	11	13	1	4.5	15	0.36
							10	14	28	3.6

NOTE.—These properties are derived using the three-dimensional model in Table 2. Quantities based on the H I line Zeeman observations are listed according to analysis of 27 emission lines or 12 absorption lines. Quantities based on optical polarization observations are computed using the parameter $s = 0.40$. The three-dimensional field direction is given in eq. (39).

dispersion of field line directions. As field lines follow the accumulating gas to which they are coupled toward the center of gravity, they will bend as a result of gravity faster than they can straighten as a result of radiation of Alfvén waves. If the accumulation occurs with nonzero angular momentum, then twisting and more complex distortions of the field can also be expected. Thus enhanced dispersion of polarization may be a signature of the "supercritical" mode of star formation described by Shu, Adams, & Lizano (1987).

On the other hand, the quiescent dark cloud filaments near clusters have polarization directions with relatively small dispersion, and with no particular preferred angle between their mean direction and the direction of the long axis of the filament. For consistency with the foregoing infall picture, it appears necessary that the quiescent filaments differ from their neighboring massive concentrations. Evidently the mean field can decouple from the gas accumulating onto such a filament, in order to take on a projected direction different from that of the filament. Pudritz & Gomez de Castro (1991) have suggested that large-scale hydromagnetic waves are responsible for the inconsistent alignment of field directions and cloud axes.

Furthermore, the infall speed during the accumulation of cluster gas probably cannot exceed the Alfvén speed by a factor greater than 2–3, since then the field strength observed toward Orion A, Orion B, and other clusters would be smaller than its equipartition value by a factor greater than is observed (Myers & Goodman 1988a). A model in which infall occurs at the Alfvén speed was proposed by Welch et al. (1987).

5.2. *Uniform and Nonuniform Magnetic Support of Molecular Clouds*

The polarization models of § 3 can account for the distributios of position angle observed in many cloud regions in terms of a uniform magnetic field component B_0 and a nonuniform component having a Gaussian distribution of amplitudes with dispersion σ_B, and having N correlation lengths along the line of sight. The values of s derived from the observations, typically 0.3 for clouds without clusters and 0.5 for clouds with clusters, can be used to estimate the relative energy density in uniform and nonuniform components of the magnetic field.

From equation (19) and (38), the ratio of energy density in the nonuniform and uniform components can be written as

$$\frac{\mathbf{M}_n}{\mathbf{M}_u} = \frac{DNs^2B_{0x}^2}{B_0^2}\,, \tag{40}$$

where D equals 2 for the two-dimensional model and 3 for the three-dimensional model of § 3. If $D = 3$ and on average $(B_{0x}/B_0)^2 = \frac{2}{3}$ for an isotropic distribution, then for clouds without clusters,

$$\frac{\mathbf{M}_n}{\mathbf{M}_u} = 0.08N \text{ to } 0.98N\,, \tag{41a}$$

using $s = 0.2$–0.7 as in Table 1. For embedded clusters, Table 1 gives $s = 0.4$ to 0.9, yielding

$$\frac{\mathbf{M}_n}{\mathbf{M}_u} = 0.32N \text{ to } 1.6N\,. \tag{41b}$$

Equation (41a) suggest that the nonuniform and uniform components in the typical dark cloud region can have comparable energy density for $1 \lesssim N \lesssim 10$, similar to the result in § 4.2 based on combining polarization and Zeeman measurements for L204. However equation (41b) indicates that for embedded cluster a smaller range, $1 \lesssim N \lesssim 3$, is needed for equal energy density in the uniform and nonuniform components.

It has long been thought that magnetic fields can support molecular clouds (e.g., Chandrasekhar & Fermi 1953; Arons & Max 1975; Shu, Adams, & Lizano 1987). Myers & Goodman (1988a, b) presented evidence for magnetic support, based on Zeeman observations, line widths, and map sizes, and on a model of equipartition between magnetic, kinetic, and gravitational energy densities. But geometrical aspects of magnetic support are still unclear. If the uniform component dominates, it is hard to explain why the nonthermal line widths have equipartition values, and how most clouds are supported along field lines. If the nonuniform component dominates, it is hard to account for the partly uniform character of optical polarization maps, and for the measurement of energetically significant line-of-sight field strengths via the Zeeman effect. These concerns suggest that the uniform and nonuniform field components may have comparable energy densities in many self-gravitating clouds (Shu, Adams, & Lizano 1987, Myers & Goodman 1990).

The results presented here clarify this picture. The optical polarization measurements indicate consistency with equal energy density in the uniform and nonuniform components, if the number N of field correlation lengths along the line of sight is 1–12 for clouds without clusters and 1–3 for clouds with clusters. For several clouds, the spatial pattern of optical polarization angles indicates several correlation lengths across the cloud, and thus on average a comparable number along the line of sight. If the field variations arise from hydromagnetic waves, the maximum value of N is 12–14. Therefore, the results presented here constitute evidence for rough consistency between optical polarization data and the partition of magnetic energy needed for cloud support.

5.3. *Sampling*

In the data presented here, three kinds of sampling nonuniformity are present: (1) Maps have small-scale nonuniformity, because the background stars lie on an irregular grid. This nonuniformity is unavoidable, but has little effect on the distribution if the sampling is fine enough. (2) Maps have differing surface density of data points from the part of a complex to another. This arises most commonly when data sets from different studies are combined—for example, in the composite Taurus map in Figure 3 of Goodman et al. (1990). This nonuniformity can have significant effects, as discussed in § 2.4. One could correct this nonuniformity by appropriate deletion of points from the denser samples. (3) Maps have large-scale "gaps" where no polarization was measured, either because the extinction is too great, or because the gap region was judged to contain too little gas to be part of the complex, or for other reasons. This nonuniformity can lead to an incomplete description of the polarization of a complex. Sampling of the higher extinction regions can be done with infrared polarimetry, while sampling of the lower extinction regions can be done with optical polarimetry.

When optical polarizatation data are combined with Zeeman mapping data as in § 4, the resulting conclusions are valid only if the magnetic field has the same uniform component, and if its nonuniform component obeys the same distribution, on the two scales at which the observations were made. For optical polarization data sampled over tens of arcminutes and for most single-antenna H I Zeeman measurements sampled every beamwidth, these sampling rates are similar.

5.4. *Field Directions and Cloud Axes*

The filamentary dark clouds in Taurus, Ophiuchus, Lupus, and other regions have a wide variety of orientation, with respect to the local mean position angle of optical polarization (Goodman et al. 1990; Scalo 1990). This variety may cast doubt on the optical polarization as a probe of the magnetic field, since one might expect a cloud with a significant magnetic field to display approximate cylindrical symmetry with respect to the mean field direction.

On the other hand, the typical field traced by optical polarization near dark clouds may have energy density significantly less than the energy density associated with the relatively opaque part of the cloud. Around L1641 and L204, field strengths of order 10 μG are indicated by Zeeman measurements of H I emission (Heiles 1987, 1988). In contrast, the field strengths in the more opaque parts of dark clouds are closer to the equipartition value of about 30 μG, according to OH measurements of the Zeeman effect in absorption in W22 (Crutcher, Kazès, & Troland 1987) or in emission in B1 (Goodman et al. 1989). Thus, the energy density in the material that defines the axis of a filamentary dark cloud might be an order of magnitude greater than the energy density in the material where the optical polarization is seen.

If so, the field direction in the denser, more opaque part of the cloud need not be constrained to align with the peripheral field indicated by the optical polarization. Infrared polarimetry of dark cloud regions may reveal the mean direction of the magnetic field in the more interior region of dark clouds with well-defined geometrical shapes. So far, the regions mapped appear to have infrared polarization directions similar to the optical polarization directions (Jones, Hyland, & Bailey 1984; Hodapp et al. 1988), but more data are needed for a definite conclusion.

If infrared and optical polarization directions agree closely in most dark clouds, and also lie at a wide range of direction with respect to the symmetry axes of the dark clouds, then it would appear that the field energy density in the typical dark cloud is at least slightly less than the gravitational energy density, despite the appearance of equipartition in some cases.

5.5. *Time Scales for Field Fluctuation and Grain Alignment*

If the shortest time scale of field fluctuations $t_{\Delta B}$ is shorter than the time scale $t_{\rm align}$ required for a grain to align with a new field direction, then the grains will be unable to follow the fastest field fluctuations.

We estimate these time scales from $t_{\Delta B} = \pi\tau_{\rm ni} = \pi/(C\gamma m^{1/2} m^{1/2})$, based on equations (26)–(27), where m is the mean molecular mass and n is the gas density, which we take to be 10^2–10^3 cm^{-3}. We take $t_{\rm align} = D\mu a^2 T B^{-2}$ from Purcell (1979). Here $D = 8.9 \times 10^3$ yr; μ is the mass density of the grain, in g cm^{-3}, which we take to be 1–2; a is the short dimension, in centimeters, of a grain with sides $a \times 2a \times 2a$, which we take to be (5–10) $\times 10^{-6}$. T is the grain temperature, which we take to be 10–20 K, and which must exceed the gas temperature. B is the field strength in gauss which we take to be (5–10) $\times 10^{-6}$. Then $t_{\Delta B}$ = (5–20) $\times 10^4$ yr, while $t_{\rm align}$ = (2–100) $\times 10^4$ yr. The time scales are comparable, but their uncertainties are too large to allow a definite conclusion.

If the optical polarization fails to reveal the faster fluctuations in the magnetic field direction, the model presented here will underestimate the nonuniform component of field energy, and a smaller number N of field correlation lengths along the line of sight will be needed for equality of uniform and nonuniform energy densities. More detailed estimates of this effect would be useful.

6. SUMMARY

The main points presented in this paper are the following:

1. The spatial distribution of polarization angle is summarized for 15 dark clouds that lack prominent star formation, for four star clusters embedded in dark clouds, for one evolved cluster with little associated extinction, and for six dark cloud complexes.
2. Most clouds have either one well-defined mean direction over their spatial extent, or two or three spatial zones having noticeably different mean directions.
3. Nearly all regions have a single local maximum in their number distribution of polarization angle. The dispersion about the mean is 0.2–0.9 radians, significantly greater than can be attributed to measurement uncertainty.
4. Clouds with embedded clusters have a more complex distribution of polarization direction than do clouds without clusters. Clouds with clusters have distributions with significantly greater breadth, and with significantly different mean direction, than do their neighboring clouds without prominent star formulation. The median cloud with an embedded cluster has dispersion 0.4–0.5 radians, while the median cloud without a cluster has dispersion 0.2–0.3 radians.
5. The median cloud with an embedded cluster has greater dispersion than does the α Persei cluster, a relatively large evolved cluster with little associated gas and dust. This suggests that the enhanced dispersion of polarization angle in clusters may be more closely associated with young stars, and/or with dense gas, than simply with the number of stars in the cluster.
6. The greatest dispersion in direction among clouds without clusters, 0.7 radians, occurs in L1689 in Ophiuchus. L1689 lies near the L1688 cloud and its embedded cluster. After L1688, L1689 has the greatest mass and extinction in Ophiuchus, but it has too few stars to be considered a cluster. This suggests that the enhanced dispersion in polarization angle in clusters may be more closely associated with dense gas than with young stars.
7. Enhanced bending and other distortions of magnetic field lines can be expected in regions where accumulation of gas has occurred, or is still occurring, with infall speeds comparable to or greater than the Alfvén speed. In this "supercritical" case the field lines bend faster as a result of gravity than they can straighten as a result of radiation of Alfvén waves.
8. Models of the distribution of electric polarization are presented in which the magnetic field at any point in a cloud consists of a straight, uniform component, with projection B_{0x}, on the plane of the sky and a nonuniform component. The nonuniform component has a Gaussian distribution of amplitude with dispersion σ_B, and an isotropic distribution of direction, in either three space dimensions or in the two dimensions perpendicular to the direction of the uniform component. The nonuniform component has N correlation lengths along the line of sight through the cloud.
9. The model predicts the probability distribution of electric polarization direction, depending on the parameters $\bar{\Theta}_E$, the

mean direction over the cloud, and on

$$s = \frac{\sigma_B}{N^{1/2} B_{0x}} ,$$

which is very nearly the rms dispersion of the distribution.

10. For s small compared with unity, the models whose nonuniform component is isotropic either in two or in three dimensions differ negligibly from each other. For $s \gtrsim 1$, the three-dimensional model f^{3D} has a central maximum, while the two-dimensional model f^{2D} has a plateau with a slight central minimum. The observed distributions with large s are better fitted by f^{3D} than by f^{2D}.

11. The spatial patterns of optical polarization suggest that N, the number of field correlation lengths along the line of sight, is of the order of a few in many clouds. An upper limit on N can be estimated if the nonuniform component arises from hydromagnetic waves: in regions with field strength 10 μG and visual extinction 1 mag, $N_{\max} \simeq 7$. If a region has equal magnetic and gravitational energy density, $N_{\max}$ is a constant of the same order as the ratio of ambipolar diffusion and free-fall time scales, about 12.

12. A map of the line-of-sight component of the magnetic field in a cloud region, from observations of the Zeeman effect, can be combined with observations of the distribution of polarization angle, to describe the three-dimensional uniform field $\boldsymbol{B}_0$. The magnitude of $\boldsymbol{B}_0$ can be completely specified, and its direction can be specified apart from a sign ambiguity in the plane-of-the-sky component. The magnitude of the total field, including the uniform and nonuniform components, can be specified in terms of N. For the dark cloud region L204, $B_0 = 6$ μG, its inclination to the line of sight is 47°, and the nonuniform and uniform components of the field energy density are equal if $N = 4$.

13. Among the clouds considered here, the range of the optical polarization dispersion s is 0.2–0.7 for clouds without clusters and 0.3–0.9 for embedded clusters. These correspond to equal energy density in the nonuniform and uniform components if N lies in the range 1–12 clouds without clusters and in the range 1–3 for embedded clusters. These estimates are consistent with upper limits on N, estimated to be of order 10 if the field nonuniformities arise from hydromagnetic waves.

We thank F. Vrba for kindly communicating data from Vrba et al. (1991) in advance of publication, and for helpful discussions. We thank P. Bastien, C. Heiles, T. J. Jones, J. M. Moran, and E. Zweibel for helpful discussions, and L. Greenhill for valuable advice on data processing. This work was partly supported by a grant to the authors from the Smithsonian Institution Scholarly Studies Program.

REFERENCES

Abramowitz, M., & Stegun, I. 1965, Handbook of Mathematical Functions (New York: Dover)
Arons, J., & Max, C. E. 1975, ApJ, 196, L77
Chandrasekhar, S., & Fermi, E. 1953, ApJ, 118, 113
Coyne, G. V., Tapia, S., & Vrba, F. J. 1979, AJ, 84, 356
Crutcher, R. M., Kazès, I., & Troland, T. H. 1987, A&A, 181, 119
Davenport, W. B., & Root, W. L. 1958, An Introduction to the Theory of Random Signals and Noise (New York: McGraw-Hill)
Davis, L. 1951, Phys. Rev., 81, 890
Davis, L., & Greenstein, J. L. 1951, ApJ, 114, 206
Elmegreen, B. G. 1978, ApJ, 225, L85
Goodman, A. A., Bastien, P., Myers, P. C., & Menard, F. 1990, ApJ, 359, 363
Goodman, A. A., Crutcher, R. M., Heiles, C., Myers, P. C., & Troland, T. H. 1989, ApJ, 338, L61
Hall, J. S. 1949, Science, 109, 166
Heiles, C. 1987, in Interstellar Processes, ed. D. J. Hollenbach & H. A. Thronson (Dordrecht: Reidel), 171
———. 1988, ApJ, 324, 321
Heyer, M. H., Vrba, F. J., Snell, R. L., Schloerb, P. F., Strom, S. E., Goldsmith, P. F., & Strom, K. M. 1987, ApJ, 321, 855
Hildebrand, R. H. 1988, QJRAS, 29, 327
Hiltner, W. A. 1949, Science, 109, 165
———. 1956, ApJS, 24, 389
Hodapp, K. W. 1987, A&A, 172, 304
Ichikawa, T., & Nishida, M. 1989, AJ, 97, 1074
Jokipii, J. R., & Parker, E. N. 1969, ApJ, 155, 799
Jones, R. V., & Spitzer, L. 1967, ApJ, 147, 943
Jones, T. J. 1989, ApJ, 346, 728
Jones, T. J., Hyland, A. R., & Bailey, J. 1984, ApJ, 282, 675
Krautter, J. 1990, paper presented at ESO Workshop on Low Mass Star Formation and Pre–Main-Sequence Objects (Garching 1989), preprint
Loren, R. B. 1989, ApJ, 338, 902
Mathewson, D. S., & Ford, V. L. 1970, MmRAS, 74, 139
McCutcheon, W. H., Vrba, F. J., Dickman, R. L., & Clemens, D. P. 1986, ApJ, 309, 619
McDavid, D. 1984, ApJ, 284, 141
Moneti, A., Pipher, J. L., Helfer, H. L., McMillan, R. S., & Perry, M. L. 1984, ApJ, 282, 508
Mouschovias, T. C. 1987, in Physical Processes in Interstellar Clouds, ed. G. Morfill & M. Scholer (Dordrecht: Reidel), 472
Myers, P. C., & Goodman, A. A. 1988a, ApJ, 326, L27
———. 1988b, ApJ, 329, 392
———. 1990, in Galactic and Intergalactic Magnetic Fields, ed. R. Beck, P. Kronberg, & R. Wielebinski (Dordrecht: Kluwer), 309
Papoulis, A. 1985, Probability, Random Variables, and Stochastic Processes (New York: McGraw-Hill)
Pudritz, R. E., & Gomez de Castro, A. I. 1991, in Fragmentation of Molecular Clouds and Star Formation, ed. E. D. Falgarone & G. Duvert (Dordrecht: Kluwer), in press
Purcell, E. M. 1979, ApJ, 231, 404
Purcell, E. M., & Spitzer, L. 1971, ApJ, 167, 31
Scalo, J. 1990, in Physical Processes in Fragmentation and Star Formation, ed. R. Capuzzo-Dolcetta, C. Chiosi, & A. DiFazio (Dordrecht: Kluwer), 151
Schneider, S., & Elmegreen, B. G. 1979, ApJS, 41, 87
Schwartz, R. D. 1977, ApJS, 35, 161
Shu, F. H., Adams, F. C., & Lizano, S. 1987, ARA&A, 25, 23
Siegel, S. 1956, Nonparametric Statistics for the Behavioral Sciences (New York: McGraw-Hill)
Tamura, M., Yamashita, T., Sato, S., Nagata, T., & Gatley, I. 1988, MNRAS, 231, 445
Taylor, K. N., & Storey, J. W. 1984, MNRAS, 209, 5P
Thompson, A. R., Moran, J. M., & Swenson, G. R. 1986, Interferometry and Synthesis in Radio Astronomy (New York: Wiley) (TMS)
Turnshek, D. A., Turnshek, D. E., & Craine, E. R. 1980, AJ, 85, 1638
Vrba, F. J., Coyne, G. V., & Tapia, S. 1981, ApJ, 243, 489 (VCT)
Vrba, F. J., Marraco, H. H., Strom, S. E., Strom, K. M., & Tamura, M. 1991, in preparation
Vrba, F. J., Strom, S. E., & Strom, K. M. 1976, AJ, 81, 958
———. 1988, AJ, 96, 680
Welch, W. J., Dreher, J. W., Jackson, J. M., Terebey, S., & Vogel, S. N. 1987, Science, 238, 1550
Wilking, B. A., Lada, C. J., & Young, E. T. 1989, ApJ, 340, 823
Zweibel, E. 1990, ApJ, 362, 545